RSC Advances

PAPER

View Article Online
View Journal | View Issue

Cite this: *RSC Adv.*, 2019, **9**, 34995

Hierarchical $NiCo_2O_4$/NiFe/Pt heterostructures supported on nickel foam as bifunctional electrocatalysts for efficient oxygen/hydrogen production†

Qingyou Huang,[a] Yang Cao,[cd] Xiaohong Wang,[d] Jinchun Tu,[d] Qianfeng Xia*[b] and Qiang Wu*[a]

Received 3rd September 2019
Accepted 24th October 2019

DOI: 10.1039/c9ra07012e

rsc.li/rsc-advances

As the demand for clean and renewable energy increases, high-efficiency multifunctional electrocatalysts for water cracking have become a research hotspot. In this study, a $NiCo_2O_4$/NiFe/Pt composite with a hierarchical structure was successfully constructed by combining a hydrothermal growth and electrodeposition method with nickel foam as the scaffold material, and its overall water cracking reaction was studied. The laminar-structured $NiCo_2O_4$/NiFe composite exhibits an improved number of electrochemically active sites and shorter electron transport pathways, while the Pt particles deposited on the $NiCo_2O_4$/NiFe composite are conducive to improve the hydrogen evolution reaction without affecting the efficiency of the oxygen evolution reaction of the intrinsic material. The $NiCo_2O_4$/NiFe/Pt composite shows an excellent overall water cracking performance under alkaline conditions with a current density of 10 mA cm^{-2} at an applied potential of 1.45 V, indicating a promising research prospect.

1. Introduction

With the rapid development of the global economy, energy dilemmas and environmental pollution have become increasingly prominent.[1] Environmental pollution is worsening due to the over-reliance on fossil energy such as oil, coal, and natural gas. Hydrogen has become an ideal alternative to fossil fuel energy, because it is environmentally friendly, abundant, and has a high energy density, and it can also be used for large-scale storage and transportation. However, it is an intermittent renewable source of energy.[2,3] Electrocatalytic water cracking, as a new kind of hydrogen energy technology, has been widely considered as a clean, sustainable and promising hydrogen production method from aqueous solution.[4,5] Water cracking reactions generally include two half-reactions. The hydrogen evolution reaction (HER) and oxygen evolution reaction (OER) need a large overvoltage.[6,7]

In recent years, big progress has been made for commonly used transition metal oxides, hydroxides, phosphates, transition metal selenides, sulfides and nitrides.[8–17] However, the optimal working conditions for these materials are often inconsistent with OER catalysts, and OER is optimized in alkaline or neutral solutions in acidic media, which requires complex steps of overall water cracking. Therefore, it is attractive but also challenging to develop a high-performance dual-function electrocatalyst with better HER and OER performance under the same conditions, which can improve the integration and simplification of water cracking and increase the feasibility of industrial applications. At present, the commonly used methods to reduce the semi-reactive overpotential include the vacancy method, doping method, and tension method.[18–20] However, these methods often lead to the contradictory combination of the two catalysts, resulting in poor splitting performance.[21–23] Heterogeneous structure has many applications in the field of catalysis. In recent years, many studies have attempted to improve water splitting by using heterogeneous structure.[24–26] Zhang *et al.*[27] synthesized MoS_2/Ni_3S_2 with a heterogeneous structure, which showed good overall water splitting performance. Here, we successfully constructed a hierarchical $NiCo_2O_4$/NiFe/Pt complex with nickel foam (NF) as the scaffold material by combining of hydrothermal growth and electrodeposition method (Fig. 1), and we used it as an effective bifunctional catalyst for HER and OER reactions. NF usually has very large pores (>200 m). $NiCo_2O_4$ is abundant and environmental friendly. It has

[a]Key Laboratory of Emergency and Trauma of Ministry of Education, Research Unit of Island Emergency Medicine of Chinese Academy of Medical Sciences, Hainan Medical University, Haikou, Hainan 571199, P. R. China. E-mail: wuqiang001001@aliyun.com
[b]Key Laboratory of Tropical Translational Medicine of Ministry of Education, School of Tropical Medicine and Laboratory Medicine, Hainan Medical University, Haikou, Hainan 571199, P. R. China. E-mail: xiaqianfeng@sina.com
[c]Qiongtai Normal University, Haikou 571127, Hainan, P. R. China
[d]State Key Laboratory of Marine Resource Utilization in South China Sea, School of Materials Science and Engineering, Hainan University, Haikou 570228, P. R. China

† Electronic supplementary information (ESI) available. See DOI: 10.1039/c9ra07012e

excellent electrochemical activity, and has twice the electrical conductivity of a single nickel or cobalt oxide based material, making it a suitable substrate material.[28] Moreover, it has more specialized nanostructured multi-layered porosity can be created by selecting appropriate preparation methods and optimization. NiFe is one of the best known OER catalysts in alkaline solutions, and the synthesized sheet structure provides more OER reaction interfaces with abundant catalytic sites.[29] On the basis of the electrodeposition of Pt, ensuring a close contact and strong coupling interface not only greatly improves the overall performance of HER and its excellent conductivity but also facilitates electronic transmission, improving the performance of mixed electrodes in alkaline KOH electrolyte. Only 1.45 V split water performance can be achieved at 10 mA cm^{-2} current.

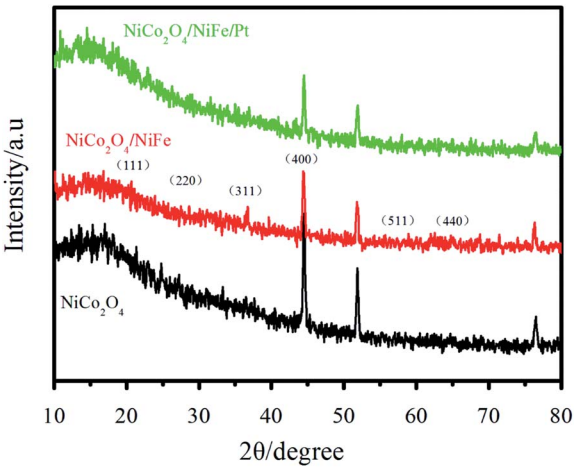

Fig. 2 XRD patterns of the $NiCo_2O_4$, $NiCo_2O_4$/NiFe, and $NiCo_2O_4$/NiFe/Pt nanostructures on NF.

2. Experimental section

2.1 The synthesis of the samples

Based on the previous report,[30] the $NiCo_2O_4$/NiFe/Pt composite can be grown on NF by a two-step hydrothermal method followed with the electrochemical deposition of Pt nanoparticles. Firstly, the NF washed with 1.0 M of HCl solution, deionized water, and anhydrous ethanol was immersed into a teflon-lined stainless steel containing 67.5 mL of $NiCl_2 \cdot 6H_2O$ (4.5 mmol), $CoCl_2 \cdot 6H_2O$ (9 mmol), and urea (13.5 mmol) aqueous solution, and then performed the hydrothermal reaction at 120 °C for 8 h to obtain the precursor. The NF/$NiCo_2O_4$ sample can be prepared by annealing the precursor at 400 °C for 3 h in the air atmosphere. Then, the obtained NF/$NiCo_2O_4$ sample was immersed into a aqueous solution containing 100 mL of 9 mmol $Ni(NO_3)_2 \cdot 6H_2O$, 3 mmol $Fe(NO_3)_3 \cdot 9H_2O$, 20 mmol urea, and 1 mmol $Na_3C_6H_5O_7 \cdot 2H_2O$, and conducted the second hydrothermal reaction at 150 °C for 48 h. After cooling to room temperature, the NF was washed with deionized water and ethanol several times to obtain the NF/$NiCo_2O_4$/NiFe sample. Finally, $NiCo_2O_4$/NiFe/Pt was synthesized by an electrochemical deposition method in the 1% H_2PtCl_6 solution at −0.2 V for 30 s.

2.2 Material characterization

The crystal structure and chemical composition of the samples were characterized by X-ray diffraction (XRD) with 40 kV voltage, 30 mA current, Cu Kα radiation (k = 1.5406 Å). The microstructure and morphology were observed on a JEOL-2100F transmission electron microscope (TEM) equipped with an energy dispersive X-ray spectrometer and a TESCAN MIRA3 field emission scanning electron microscope (SEM). X-ray photoelectron spectroscopy (XPS) was applied to study the surface chemical composition and valence of the samples.

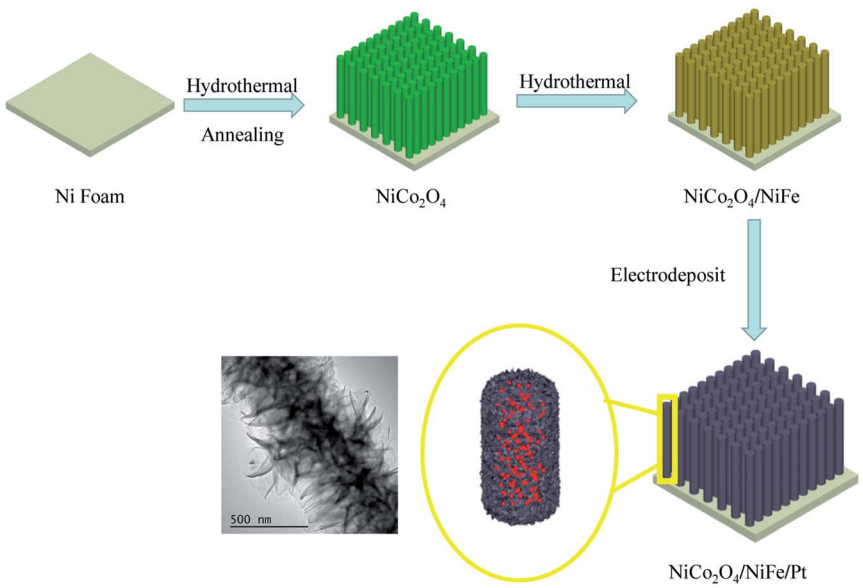

Fig. 1 Schematic of the facile synthesis of $NiCo_2O_4$/NiFe/Pt heterogeneous structure nanowire arrays grown on NF substrate.

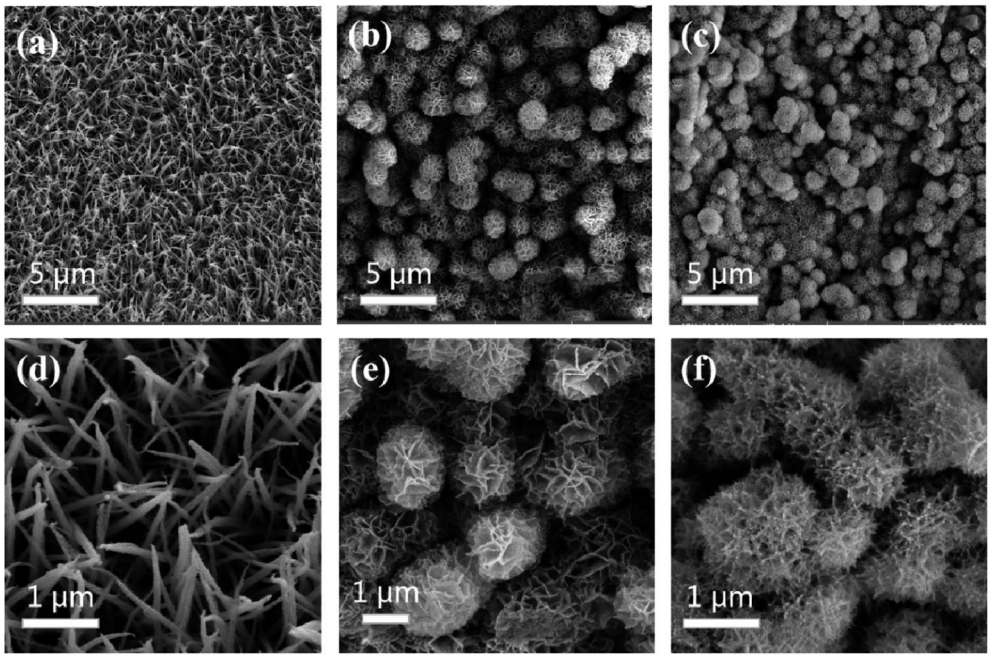

Fig. 3 SEM images of $NiCo_2O_4$ arrays (a and d), $NiCo_2O_4$/NiFe arrays (b and e), and $NiCo_2O_4$/NiFe/Pt arrays (c and f) on NF at different magnifications.

2.3 Electrochemical measurements

All electrochemical experiments were carried out at room temperature by a VMP-300 electrochemical workstation in 1 M KOH aqueous electrolyte. The saturated calomel electrode (SCE) was used as reference electrode, the platinum wire was served as the counter electrode, and the synthesized $NiCo_2O_4$/NiFe/Pt complex was utilized as working electrode. To assess the HER performance of the samples, linear sweep voltammetry (LSVs) were measured from −0.5 V to −1.4 V *versus* saturated SCE with a scan rate of 5 mV s^{-1}. To evaluate the OER performance samples, LSVs were measured from 0 V to 0.7 V *versus* SCE at a scan rate of 2 mV s^{-1}. Chronopotentiometry measurements were performed at current densities of 10, 30, and 50 mA cm^{-2} for 30 h, and the potential was converted to RHE scale by the formula $E_{RHE} = E_{SCE} + 0.059 \times pH + 0.245$, where E_{RHE} is the potential *versus* RHE and E_{SCE} is the measured potential refer to the SCE reference electrode. The overpotentials were obtained through the intersection point of the tangent lines of LSV current and the polarization curve baseline.

3. Results and discussion

To further investigate the phase structures of $NiCo_2O_4$/NiFe/Pt, the XRD patterns of the as-prepared own in Fig. 2. It could be seen in Fig. 2 that the peaks at 19.5°, 31.1°, 36.7°, 44.6°, 59.0°, and 64.8° corresponded to the (111), (311), (400), (511), and (440) planes of the spinel $NiCo_2O_4$, respectively (JCPDS card no. 20-0781).[30,31] The lack or very low reflection intensity of NiFe in the hybrid products were mainly due to its low crystallinity and ultrathin property. In this hydrothermal system, after $NiCo_2O_4$ surface reaction for a period of time, NiFe crystallization degree was relatively low without annealing treatment. Herein, the reflections corresponding to stratification would be very weak or even could not be detected in the observation process.

Fig. 3(a) and (d) revealed the SEM images of $NiCo_2O_4$ arrays on NF at different magnifications. Fig. 3(a) indicated a large number of needle-like $NiCo_2O_4$ arrays grown vertically along the surface of the NF, with a large surface area and a stable porous three-dimensional spatial structure. Fig. 3(d) showed that the average diameter of the $NiCo_2O_4$ arrays was about 100 nm. While the NiFe was introduced with hydrothermal process, core/shell structure was observed (Fig. 3(b)). Due to the growth of a layer of interconnecting NiFe nanosheets on the thin $NiCo_2O_4$ array, the surface of the array turned very rough. Apparently, the layer reflected a degree of folds (Fig. 3(e)), thus increasing the surface area. Finally, Pt nanoparticles were successfully deposited on the NiFe nanosheet by electrodeposition, as is shown in Fig. 3(c), and the thickness of Pt nanoparticles was about several tens of nanometers (inset of Fig. 3(f)). As a result, the surface area could be improved and large amounts of active sites could be occurred for the Faraday process.

The structure of hybrid products was further studied by TEM. In Fig. 4(a) and (b), the diameter of $NiCo_2O_4$ nanowire was approximate 100 nm, which was resemble to the SEM image (Fig. 3(d)). The nanowire was made up of numerous interconnected nanoparticles, which could be on account of the release of gas during the calcination treatment. It could be seen that the high-resolution TEM (HRTEM) image (Fig. 4(c)) demonstrated that the spacing of the lattice plane was about 0.25 nm, which could be ascribed to the (311) crystal planes of the $NiCo_2O_4$ phase. In Fig. 4(d) and (e), the $NiCo_2O_4$ nanowires were embellished with ultrathin NiFe nanosheets. The hierarchical core/shell nanostructure could not only guarantee

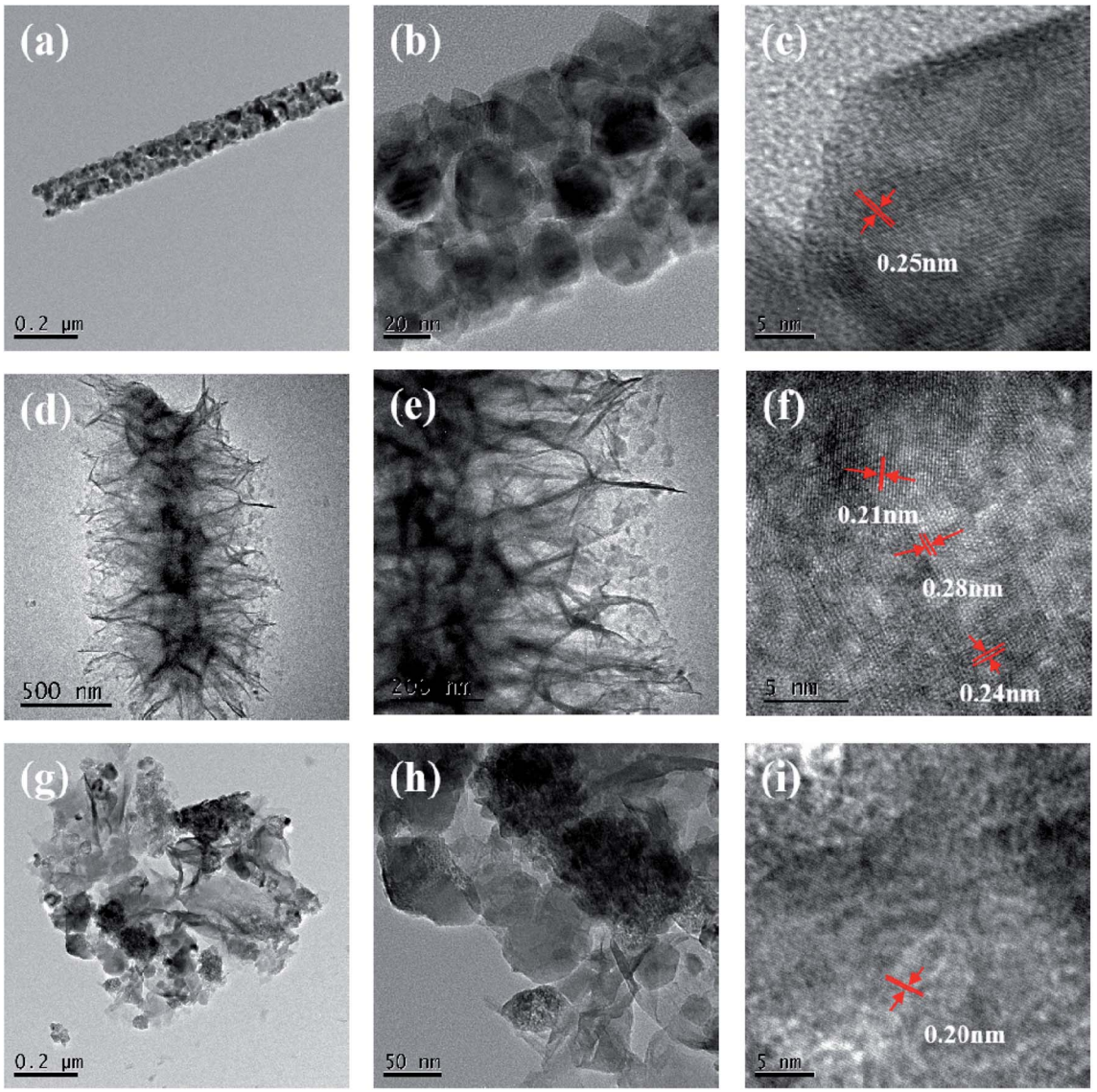

Fig. 4 TEM (a and b) and HRTEM images (c) of the $NiCo_2O_4$ nanowire. TEM (d and e) and HRTEM images (f) of the $NiCo_2O_4$/NiFe arrays. TEM (g and h) and HRTEM images (i) of the $NiCo_2O_4$/NiFe/Pt arrays.

powerful interaction with each other, but also supply a large surface area and enough active sites for redox reactions. The HRTEM image in Fig. 4(f) showed that the distance between two adjacent lattices was approximately 0.21, 0.24, and 0.28 nm, which were consistent with the (400), (311), and (220) planes of $NiCo_2O_4$ phase, respectively. In Fig. 4(g) and (h), the Pt nanoparticles were successfully deposited on the ultrathin NiFe nanosheets, the diameter is about 100 nm. The energy dispersive X-ray spectra (EDS) for $NiCo_2O_4$/NiFe/Pt arrays are shown in Fig. S2,† demonstrates that the arrays are mainly constituted by O, Fe, Co, Ni, and Pt elements. The EDS results confirmed the formation of Pt nanoparticles and attachment on $NiCo_2O_4$/NiFe with a weight fraction of about 7.64%. The HRTEM image in Fig. 4(i) revealed that the measured distance between two adjacent lattices was approximately 0.20 nm, which was consistent with the (200) plane of Pt phase.

The detailed elemental mapping images could be seen in Fig. 5(a), which depicted the homogeneous distribution of Ni, Co, Fe, and Pt atoms on the surface of the distinct heterostructures. XPS was tested to discuss the chemical states of $NiCo_2O_4$/NiFe/Pt heterostructures and explore the bonding state of elements and conceivable coupling between the components. The XPS spectrum of Ni 2p (Fig. S1a, ESI†) manifested that the Ni atoms in Ni $2p_{1/2}$ and Ni $2p_{3/2}$ electronic configurations occurred at 873.0 and 855.2 eV, respectively, which suggested the Ni^{2+} in $NiCo_2O_4$. Relatively, the peaks located at 875.0 and 856.7 eV were geared to Ni^{3+}.[31,32] As is seen in Fig. 5(b), not only the peaks of Co $2p_{1/2}$ located at 797.1 eV and Co $2p_{3/2}$ located at 781.5 eV but also the spin-energy separation of 15.6 eV could confirm the existence of both Co^{2+} and Co^{3+}.[33,34] It could be seen in Fig. 5(c) that the XPS spectrum of Fe 2p exhibited two peaks located at 713.2 and 726.0 eV for

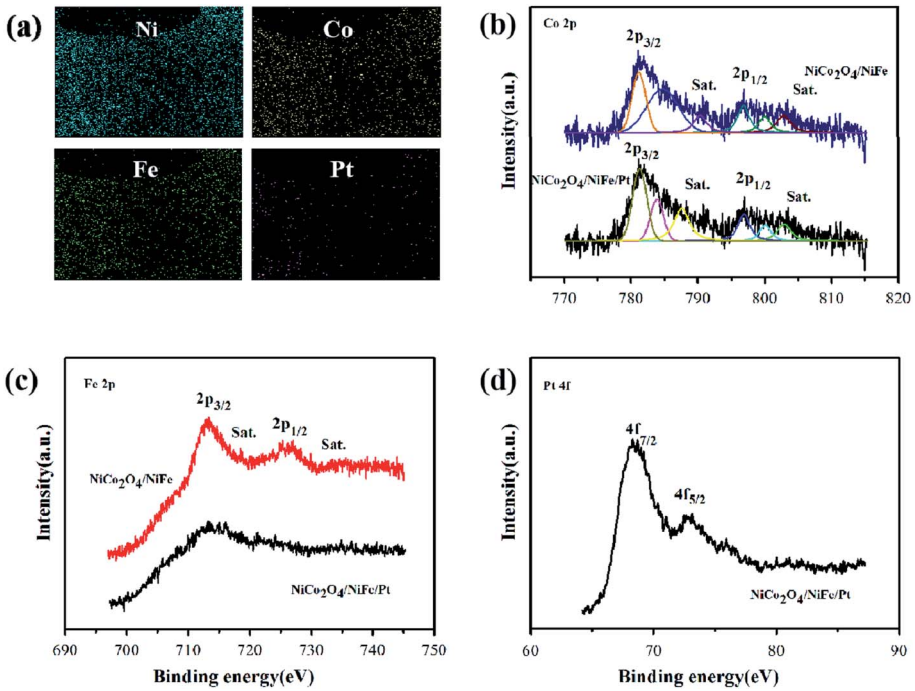

Fig. 5 Elemental mapping images (a). XPS characterization of $NiCo_2O_4$/NiFe and $NiCo_2O_4$/NiFe/Pt hybrid; high-resolution XPS spectra for (b) Co 2p, (c) Fe 2p, and (d) Pt 4f.

$NiCo_2O_4$/NiFe, which corresponded to Fe $2p_{3/2}$ and $2p_{1/2}$, respectively. But there was a difference for $NiCo_2O_4$/NiFe/Pt that the XPS spectrum of Fe 2p exhibited two peaks located at 713.5 and 726.2 eV, existed a certain deviation. It can be seen that chemical interaction, rather than physical adsorption, occurs between Pt and the material. In addition, the peaks located at 718.7 and 733.7 eV confirmed the existence of Fe^{3+} oxidation state of NiFe nanosheets.[28] In Fig. 5(d), the XPS spectrum indicated that the Pt 4f in 4f $_{7/2}$ and 4f $_{5/2}$ electronic configurations appeared at 68.4 and 72.7 eV, respectively, and the spin-energy separation occurred at 4.3 eV.[35] Herein, on the basis of the XPS discussed above, the surface of the $NiCo_2O_4$/NiFe/Pt/NF

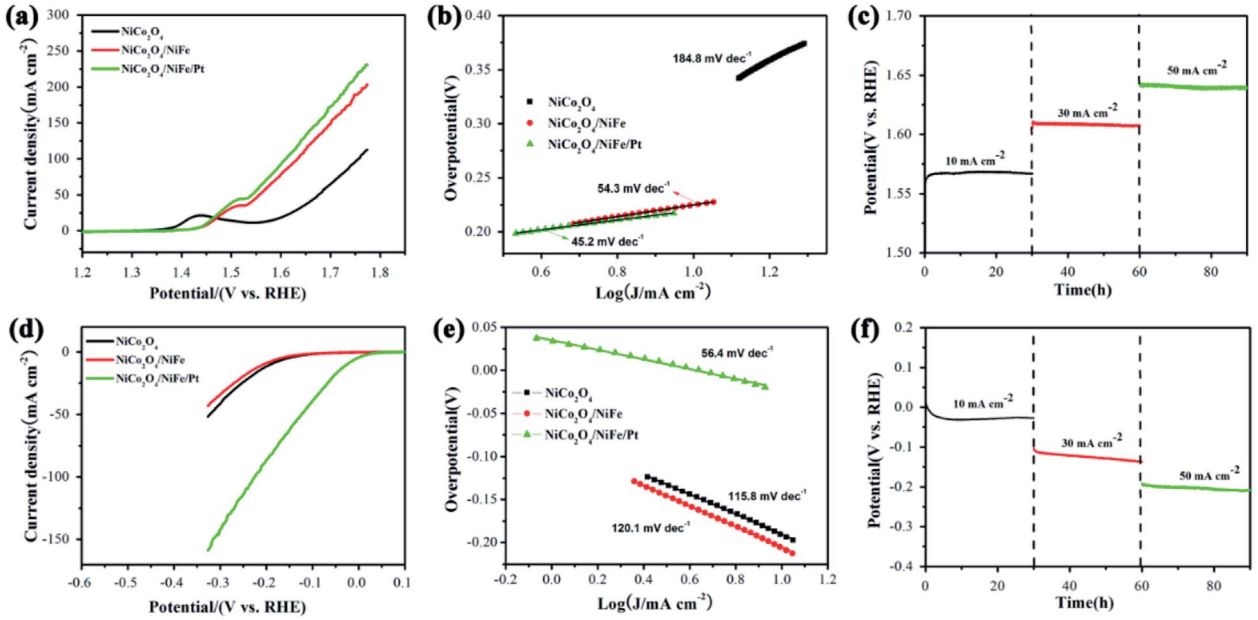

Fig. 6 Bifunctional catalytic performance of $NiCo_2O_4$/NiFe/Pt hybrid electrode on NF in 1.0 M aqueous KOH electrolyte. OER: (a) anodic polarization curves, (b) corresponding Tafel plots, and (c) chronopotentiometry curve. HER: (d) cathodic polarization curves, (e) corresponding Tafel plots, and (f) chronopotentiometry curves.

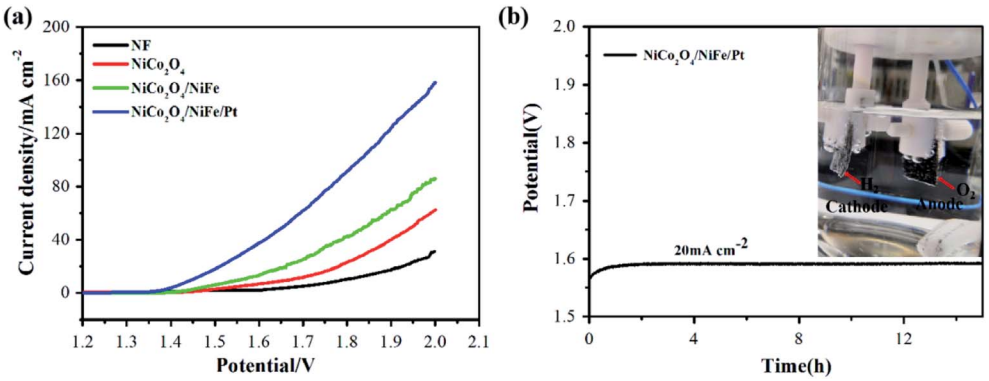

Fig. 7 Overall splitting performance. (a) Polarization curves of overall water splitting for $NiCo_2O_4$/NiFe/Pt hybrid electrode compared with those of the respective component and bare NF at a scan rate of 5 mV s^{-1} in 1.0 M aqueous KOH. (b) Chronopotentiometry curve of water electrolysis for the hybrid electrode serving as both cathode and anode under a constant current density of 20 mA cm^{-2}. Inset: photographic image of two-electrode water electrolysis device and simultaneous evolution of H_2 and O_2 on cathode and anode.

sample was comprised of Co^{2+}, Co^{3+}, Ni^{2+}, Fe^{3+}, and Pt. Therefore, Pt was successfully grown on the $NiCo_2O_4$/NiFe nanotube arrays.

The catalytic activities of the $NiCo_2O_4$/NiFe/Pt electrode were investigated for OER in 1 M KOH with a three-electrode system while the scan rate was kept at 2 mV s^{-1}. All potentials used to investigate were adapted to reversible hydrogen electrode (RHE). To evaluate the effect of heterostructures on the NF substrate, $NiCo_2O_4$ and $NiCo_2O_4$/NiFe were prepared at the same time, and their OER activities were detected with the same situation. The data which was shown in Fig. 6(a) revealed that $NiCo_2O_4$/NiFe/Pt emerged a higher current density, attaining 50 mA cm^{-2} at a relatively lower overpotential (η) (310 mV), which was lower than that of $NiCo_2O_4$ (446 mV) or $NiCo_2O_4$/NiFe (327 mV). Liner sweep voltammetry polarization curves indicated a huge imparity of OER activities for multifarious electrocatalysts. The Tafel slope in Fig. 6(b) was resulted from linear fitting of Tafel plots (η *vs.* log (j)) and reflected a low value of 45.2 mV dec^{-1}, additionally confirming the remarkable OER reaction kinetics of $NiCo_2O_4$/NiFe/Pt. Due to the enhanced catalytic activity and kinetics, the $NiCo_2O_4$/NiFe/Pt electrode emerged greater current density than $NiCo_2O_4$ (184.8 mV dec^{-1}) or $NiCo_2O_4$/NiFe (54.3 mV). Aside from the high OER activity, the hybrid electrode exhibited superb stability under alkaline conditions. The electrochemical durability for electrolysis of water oxidation which was performed at constant catalytic current densities revealed that stable overpotential was retained with degradation which could ignored in oxygen evolution for at least 90 h (Fig. 6(c)).

The HER evaluation were also discussed with a typical three-electrode configuration. In comparison with $NiCo_2O_4$/NiFe/Pt, the LSV curve of both $NiCo_2O_4$ and $NiCo_2O_4$/NiFe on NF was also presented in Fig. 6(d). The $NiCo_2O_4$/NiFe/Pt electrode demonstrated an apparent effect with an adequately low onset potential of 13 mV, which was particularly lower than that of $NiCo_2O_4$ (170 mV) and $NiCo_2O_4$/NiFe (175 mV). Furthermore, scanning toward negative potential exhibited a prompt rise in HER current density, which displayed that the $NiCo_2O_4$/NiFe/Pt could be regarded as valid cathode which could be applied not only in water reduction but also in hydrogen release. The hybrid electrode attained a 10 mA cm^{-2} current density at a negative potential of 27 mV, which demonstrated best consequence when compared with $NiCo_2O_4$ on NF (194 mV) and directly grown $NiCo_2O_4$@NiFe (205 mV),[36] NiFe-LDH/$NiCo_2O_4$,[27] NiFe/$NiCo_2O_4$/NF (105 mV),[29] TiO_2@Co_9S_8 (139 mV), and[37] $NiCo_2S_4$@NiFe LDH/NF (200 mV).[38] Furthermore, the $NiCo_2O_4$/NiFe after electrodeposition of Pt nanoparticles reflected a tremendous increase in reaction kinetics, which manifested a low Tafel slope of 56.4 mV dec^{-1} (Fig. 6(e)). The Tafel slope for $NiCo_2O_4$ (115.8 mV dec^{-1}) and $NiCo_2O_4$/NiFe (120.1 mV dec^{-1}) indicated a doughty novel synergistic effect between Pt nanoparticles and $NiCo_2O_4$/NiFe for HER. The perfect HER stability of the fresh hybrid at constant catalytic current densities revealed that stable overpotential was retained which the degradation in oxygen evolution was negligible for at least 90 h, as is shown in Fig. 6(f).

On the basis of the catalytic activities of the $NiCo_2O_4$/NiFe/Pt electrode toward OER and HER reaction, the hybrid electrode could be served as an valid and steady bifunctional electrocatalyst for not only overall water splitting but also integrated HER and OER in alkaline media. Therefore, a two-electrode device with the obtained hybrid electrode taken for electrocatalysts for both anode and cathode was established, in which a catalytic current was viewed while the applied potential was higher than 1.45 V. Larger potential induced a prompt increase in current; densities of 10 and 20 mA cm^{-2} were quickly reached at cell voltages of 1.45 and 1.51 V, respectively; and bubbles of hydrogen and oxygen were gradually formed from cathode and anode, respectively (Fig. 7(a)). Compared with $NiCo_2O_4$ and $NiCo_2O_4$/NiFe, the requested potential was lower than both of them. By contrast, the potential exceeded 1.78 V for $Ni(OH)_2$/$NiSe_2$//$Ni(OH)_2$/$NiSe_2$,[39] 1.60 V for NiFe-LDH/$NiCo_2O_4$,[27] 1.67 V for NiFe/$NiCo_2O_4$/NF,[29] 1.56 V for TiO2@Co_9S_8, and[37] 1.60 V for $NiCo_2S_4$@NiFe LDH/NF.[38] The chronopotentiometry curve at 20 mA cm^{-2} demonstrated that the overall water-splitting property was jarless for at least 15 h while the electrode was loaded with

$NiCo_2O_4$/NiFe/Pt (Fig. 7(b)). The results displayed that this hybrid nanomaterial may be a very prospective candidate catalyst which applied in water electrolysis.

Compared with other electrocatalysts, the hybrid electrode manifested well. The 3D NF with macroporous structure revealed well mechanical property, elevated surface area, excellent electrical conductivity, which could improve the diffusion between ion and electrolyte. The $NiCo_2O_4$ nanorod made up of interconnected nanoparticles guaranteed commendable mechanical and electrical contact, which could enlarge accessible active surface area. Meanwhile, it may supply open channels so that electrolyte could be diffused into active sites. Therefore, the formed H_2 or O_2 bubbles could be released rapidly. The NiFe nanosheet increased large amount of catalytic sites and decreased the reaction activation energy. Meanwhile, the reaction efficiency was enhanced. Pt nanoparticles ensured a strong coupling interface, which not only greatly improved the overall performance of hydrogen generation reaction and its excellent conductivity but also facilitated the electronic transmission, improving the performance of mixed electrodes in alkaline KOH electrolyte.

4. Conclusion

A novel hierarchical $NiCo_2O_4$/NiFe/Pt heterostructure for overall water splitting was successfully synthesized *via* hydrothermal growth and electrodeposition. The outstanding performance of the $NiCo_2O_4$/NiFe/Pt electrode is due to the distinct multilevel hierarchical catalyst architecture, including 3D NF, $NiCo_2O_4$ nanorods, NiFe double hydroxide nanosheets, and Pt nanoparticles. The hierarchical structure owed an improved surface area and active sites for electrolytic water splitting. The $NiCo_2O_4$/NiFe/Pt hybrid electrode exhibits high performance for both OER and HER, which could attain a high current density of 10 mA cm^{-2} at a low cell voltage of 1.45 V in a two-electrode system.

Conflicts of interest

There are no conflicts to declare.

Acknowledgements

This work was supported by grants from the National Natural Science Foundation of China (81860373), the Finance Science and Technology Project of Hainan Province (ZDXM2014069).

References

1 W. Wang, M. O. Tadé and Z. Shao, *Chem. Soc. Rev.*, 2015, **44**, 5371–5408.
2 M. S. Dresselhaus and I. L. Thomas, *Nature*, 2001, **414**, 332–337.
3 J. A. Turner, *Science*, 2004, **305**, 972–974.
4 M. G. Walter, E. L. Warren, J. R. McKone, S. W. Boettcher, Q. Mi, E. A. Santori and N. S. Lewis, *Chem. Rev.*, 2010, **110**, 6446–6473.
5 N. S. Lewis and D. G. Nocera, *Proc. Natl. Acad. Sci. U. S. A.*, 2006, **103**, 15729–15735.
6 X. Li, X. Hao, A. Abudula and G. Guan, *J. Mater. Chem. A*, 2016, **4**, 11973–12000.
7 J. Wang, W. Cui, Q. Liu, Z. Xing, A. M. Asiri and X. Sun, *Adv. Mater.*, 2016, **28**, 215–230.
8 H. Li, C. Tsai, A. L. Koh, L. Cai, A. W. Contryman, A. H. Fragapane, J. Zhao, H. S. Han, H. C. Manoharan, F. Abild-Pedersen, J. K. Nørskov and X. Zheng, *Nat. Mater.*, 2015, **15**, 48.
9 H. Zhou, Y. Wang, R. He, F. Yu, J. Sun, F. Wang, Y. Lan, Z. Ren and S. Chen, *Nano Energy*, 2016, **20**, 29–36.
10 Q. Liu, J. Tian, W. Cui, P. Jiang, N. Cheng, A. M. Asiri and X. Sun, *Angew. Chem., Int. Ed.*, 2014, **53**, 6710–6714.
11 X. Yan, L. Tian, S. Atkins, Y. Liu, J. Murowchick and X. Chen, *ACS Sustainable Chem. Eng.*, 2016, **4**, 3743–3749.
12 R. Chen, G. Sun, C. Yang, L. Zhang, J. Miao, H. Tao, H. Yang, J. Chen, P. Chen and B. Liu, *Nanoscale Horiz.*, 2016, **1**, 156–160.
13 E. J. Popczun, J. R. McKone, C. G. Read, A. J. Biacchi, A. M. Wiltrout, N. S. Lewis and R. E. Schaak, *J. Am. Chem. Soc.*, 2013, **135**, 9267–9270.
14 C. Zhang, J. Liu and B. Chen, *Ceram. Int.*, 2018, **44**, 19735–19742.
15 R. Li, J. Zhou, J. Liu and B. Chen, *Mater. Res. Express*, 2019, **6**, 075802.
16 C. Zhang, J. Liu and B. Chen, *Appl. Phys. A*, 2019, **125**, 150.
17 C. Zhang, J. Liu, S. Guo, S. Xiao, Z. Shen and L. Xu, *Ceram. Int.*, 2018, **44**, 14377–14385.
18 K. Fominykh, P. Chernev, I. Zaharieva, J. Sicklinger, G. Stefanic, M. Döblinger, A. Müller, A. Pokharel, S. Böcklein, C. Scheu, T. Bein and D. Fattakhova-Rohlfing, *ACS Nano*, 2015, **9**, 5180–5188.
19 Y. Liu, H. Cheng, M. Lyu, S. Fan, Q. Liu, W. Zhang, Y. Zhi, C. Wang, C. Xiao, S. Wei, B. Ye and Y. Xie, *J. Am. Chem. Soc.*, 2014, **136**, 15670–15675.
20 J. R. Petrie, V. R. Cooper, J. W. Freeland, T. L. Meyer, Z. Zhang, D. A. Lutterman and H. N. Lee, *J. Am. Chem. Soc.*, 2016, **138**, 2488–2491.
21 C. W. B. Bezerra, L. Zhang, K. Lee, H. Liu, A. L. B. Marques, E. P. Marques, H. Wang and J. Zhang, *Electrochim. Acta*, 2008, **53**, 4937–4951.
22 M. Chen, L. Wang, H. Yang, S. Zhao, H. Xu and G. Wu, *J. Power Sources*, 2018, **375**, 277–290.
23 X. Zhang and Y. Liang, *Adv. Sci.*, 2018, **5**, 1700644.
24 D. Deng, K. S. Novoselov, Q. Fu, N. Zheng, Z. Tian and X. Bao, *Nat. Nanotechnol.*, 2016, **11**, 218.
25 W. Zhao, X. Li, R. Yin, L. Qian, X. Huang, H. Liu, J. Zhang, J. Wang, T. Ding and Z. Guo, *Nanoscale*, 2019, **11**, 50–59.
26 Y. Guo, J. Tang, H. Qian, Z. Wang and Y. Yamauchi, *Chem. Mater.*, 2017, **29**, 5566–5573.
27 Z. Wang, S. Zeng, W. Liu, X. Wang, Q. Li, Z. Zhao and F. Geng, *ACS Appl. Mater. Interfaces*, 2017, **9**, 1488–1495.
28 J. Chi, H. Yu, B. Qin, L. Fu, J. Jia, B. Yi and Z. Shao, *ACS Appl. Mater. Interfaces*, 2017, **9**, 464–471.
29 C. Xiao, Y. Li, X. Lu and C. Zhao, *Adv. Funct. Mater.*, 2016, **26**, 3515–3523.

30 H. Gao, Y. Cao, Y. Chen, Z. Liu, M. Guo, S. Ding, J. Tu and J. Qi, *Appl. Surf. Sci.*, 2019, **465**, 929–936.
31 P. Xia, Q. Wang, Y. Wang, W. Quan, D. Jiang and M. Chen, *J. Alloys Compd.*, 2019, **771**, 784–792.
32 J. Liang, Z. Fan, S. Chen, S. Ding and G. Yang, *Chem. Mater.*, 2014, **26**, 4354–4360.
33 L. Ai, X. Gao and J. Jiang, *J. Power Sources*, 2014, **257**, 213–220.
34 X. Xu, J. Gao, G. Huang, H. Qiu, Z. Wang, J. Wu, Z. Pan and F. Xing, *Electrochim. Acta*, 2015, **174**, 837–845.
35 H. Chen, F. Zhang, X. Sun, W. Zhang and G. Li, *Int. J. Hydrogen Energy*, 2018, **43**, 5331–5336.
36 J. Luo, J.-H. Im, M. T. Mayer, M. Schreier, M. K. Nazeeruddin, N.-G. Park, S. D. Tilley, H. J. Fan and M. Grätzel, *Science*, 2014, **345**, 1593–1596.
37 S. Deng, Y. Zhong, Y. Zeng, Y. Wang, X. Wang, X. Lu, X. Xia and J. Tu, *Adv. Sci.*, 2018, **5**, 1700772.
38 J. Liu, J. Wang, B. Zhang, Y. Ruan, L. Lv, X. Ji, K. Xu, L. Miao and J. Jiang, *ACS Appl. Mater. Interfaces*, 2017, **9**, 15364–15372.
39 H. Liang, L. Li, F. Meng, L. Dang, J. Zhuo, A. Forticaux, Z. Wang and S. Jin, *Chem. Mater.*, 2015, **27**, 5702–5711.